Multi-objective optimisation of deployable bistable scissor structures

Arnouts, Liesbeth I.W.; Massart, Thierry J.; De Temmerman, Niels; Berke, Peter

Published in:
Automation in Construction

DOI:
10.1016/j.autcon.2020.103154

Publication date:
2020

Multi-objective optimisation of deployable bistable scissor structures

L.I.W. Arnouts[a,b], T.J. Massart[a], N. De Temmerman[b], P.Z. Berke[a,*]

[a] *Structural and Material Computational mechanics (SMC), BATir Department, Université libre de Bruxelles (ULB), 50, avenue Franklin Roosevelt, 1050 Brussels, Belgium*

[b] *Transform Research team, Department of Architectural Engineering (ae-lab), Vrije Universiteit Brussel (VUB), Pleinlaan 2, 1050 Brussels, Belgium*

Abstract

Lightweight bistable deployable structures can be designed to be transportable and reusable. They instantaneously achieve some structural stability when transformed from the compact to the deployed state through a controlled snap-through, as a result of intended geometric incompatibilities between the beams. Due to their transformable bistable nature their design requires assessing both their non-linear transformation behaviour, as well as their service state in the deployed configuration. The requirement of a low peak force during transformation can be shown to oppose the high stiffness requirement in the deployed state; their design can therefore be formulated as a multi-objective non-linear optimisation problem. In this contribution, a size and shape optimisation method is elaborated by choosing the best material combinations, the optimal geometry of the structure and beam cross-sections. The originality of this contribution is the use of a multi-objective evolutionary algorithm to structurally optimise bistable scissor structures taking into account the deployed state as well as the transformation phase. First, the method is applied to optimise a single bistable scissor module. Next, a multi-module bistable scissor structure is optimised and the single module and full structure based approaches are critically compared.

Keywords: structural engineering, non-linear computational mechanics, deployable structures, scissor structures, bistable structures, multi-objective optimisation, evolutionary algorithms

1. Introduction

Scissor structures consist of scissor-like elements (SLE), themselves made of two beams connected by a pivot connection which allows the beams rotating around an axis perpendicular to the plane of the two beams. Mobile lightweight deployable scissor structures are transportable and can be transformed rapidly while offering a huge volume expansion. Geometric incompatibilities between the members during transformation can be introduced as a design strategy to obtain bistability (i.e. stable folded and deployed states), which instantaneously introduces some structural stability in the deployed state. Zeigler was the first to propose this self-supporting concept in scissor structures [1, 2], followed by Clarke [3], Zalewski and Krishnapillai [4], Logcher and Rosenfeld [5, 6], and Gantes and Connor [7–11]. In bistable scissor structures, the intended geometric incompatibilities result in the bending of some specific members with a controlled snap-through behaviour while they are transforming from the folded to the deployed configuration. Because of the large displacements and rotations and the bistability, the transformation behaviour of bistable scissor structures, first studied computationally by Gantes [11], is highly non-linear. By consequence, both the service state as well as the transformation phase have to be considered in the design. Although analysing bistable scissor structures is a contemporary research topic [12–19], existing applications in civil engineering are rare, largely due to this complex structural behaviour.

A proper structural design has to provide sufficient stiffness in the deployed state, while providing flexibility during deployment to limit the force required for transformation, which are contradicting requirements [20]. The complex structural behaviour of bistable scissor structures, being different both during deployment and in the deployed configuration, prevents the formulation of any straightforward, rigorous and automated design methodology. A design methodology was suggested by Gantes [11, 21], the main limitation being that every iteration on the design has to be performed manually.

Because of the progress in computational efficiency over the recent years, several researchers in the field of *mechanism-type of scissor or pantographic structures* (without snap-through) used optimisation methods successfully. Sequential Quadratic Programming was first used by You to minimise the weight or maximise the stiffness of a pantographic mast in terms of the geometry, cross-sectional areas and material properties, satisfying displacement, strength and buckling constraints [22]. The folded and the deployed configuration, with and with-

*Corresponding author
Email address: pberke@ulb.ac.be (P.Z. Berke)

out prestress, were considered. Kaveh used Recursive Quadratic Programming to minimise the weight of scissor structures by varying the cross-sectional area of the beams, using penalty functions for the stress, buckling and displacement constraints [23]. He continued to optimise scissor structures using a genetic algoritm [24] and Ant Colony Optimisation [25–27]. For movable bridge design, Thrall et al. employed shape and size optimisation [28, 29]. They used Multi-Objective Simulated Annealing and the First Best Gradient method to minimise the self-weight and the power required for the operation of the bridge in terms of the geometry and the cross-sections, satisfying kinematic and structural constraints. Thrall et al. [30] presented a methodology for the size and shape optimisation of pantographic structures to minimise their weight with a Gradient-based Steepest Descent algorithm, Genetic Algorithm, Simulated Annealing and Descent Local Search. Alegria Mira et al. used Simulated Annealing and Descent Local Search to do a topology, shape and size optimisation of the Universal Scissor Component [31] to minimise its weight, satisfying the constraints of Eurocode 9 [32], as well as Descent Local Search to minimise the weight of a scissor arch in terms of the geometry [33]. Koumar et al. used for the first time the Nondominated Sorting Genetic Algorithm II to perform a multi-objective optimisation of a barrel vault, leading to a Pareto front with several optimal solutions [34, 35]. The mass and the compactness were minimised, varying the cross-section and the geometry and satisfying the constraints of Eurocode 9. Recently, Salar introduced a fast Genetic Algorithm method for the size optimisation of scissor structures to minimize their weight [36]. All of the previous methods were used to optimise stable states of scissor structures, e.g. the deployed configuration. By consequence, no non-linear analyses were required.

The *optimisation of bistable scissor structures*, which requires taking into account the geometric non-linearities during transformation, was attempted by Gantes [37]. Genetic algorithms were applied for the design of a bistable scissor structure to minimise its weight, varying the cross-sectional dimensions and material properties using penalty functions for the stress and displacement constraints, leading to one optimal design. Two problems were solved: (1) a geometrically non-linear analysis during deployment, using a quarter of a single module to predict the response of the multi-module structure and (2) a linear analysis in the deployed state. Although the proposed approach is of high interest and may be the sole precursor to this contribution, additional complementary developments are required to address fully the aspects of deployment and deployed state in a unified manner for two reasons. First, the simplification of the structure to a quarter of a single module during transformation does not take into account the correct direction of the external forces in every module nor the forces between the modules. Second, the resulting single optimal design does not allow the designer to make choices based on preferences such as the aesthetics of the structure.

Therefore, in this contribution, a *multi-objective size and shape optimisation* problem is elaborated to obtain *an optimal set of bistable structures* which provide stiffness in the deployed state and flexibility during deployment by choosing the best combinations of the geometry, of the cross-sections of the beams and of their material properties. The originality of this contribution is: (1) the development of a multi-objective optimisation methodology for bistable scissor structures, obtaining a Pareto front with several optimal solutions, (2) the incorporation of the non-linear response of the whole structure during transformation as well as its response in the deployed configuration and (3) the application of the methodology to single unit and full structure cases. A single bistable scissor module and a multi-module bistable scissor structure are optimised and the results are critically compared.

The paper is organised as follows. Section 2 explains the optimisation problem statement for bistable scissor structures. Section 3 establishes the optimisation formulation. Its computational implementation is discussed in Section 3.1. In Section 4, a single bistable scissor module is optimised and the results are discussed. In Section 5, a multi-module structure is optimised with boundary conditions that mimic the boundary conditions of the single module in Section 5.1 and with rail supports along two sides in Section 5.2 and the results are critically compared. Conclusions are given in Section 6.

2. Optimisation problem statement for bistable scissor structures

2.1. Geometry and structural response

The considered structures are a square flat polygonal module made of 8 SLE's (Fig. 1) and a multi-module assembly of such single modules (presented in Section 5). During the module transformation, the outer SLE's (on the edges of the module) remain straight while the inner SLE's (on the diagonals of the module) bend due to geometric incompatibilities. The length of the edge of the square module is 1 m and the height of the corner points of the module is chosen to be 0.33 m in the deployed state.

In general, the load-displacement curve of bistable scissor structures is similar to Fig. 2, showing the folding of a single module. The load is the sum of all the applied folding force magnitudes (i.e. not a vector sum) $F = \sum_{p=1}^{n_{forces}} F_p$ (with n_{forces} the number of forces) and the displacement is the relative vertical displacement between the center points. In this case, the lower corner points are considered to be fixed in the vertical direction z, while the upper corner points are subjected to a horizontal load in the direction of the diagonals which is fixed throughout the transformation (Fig. 3). Point A corresponds to the initial deployed configuration. Due to geometric incompatibilities, some of the beams bend elastically, requiring an increasing force to fold the structure

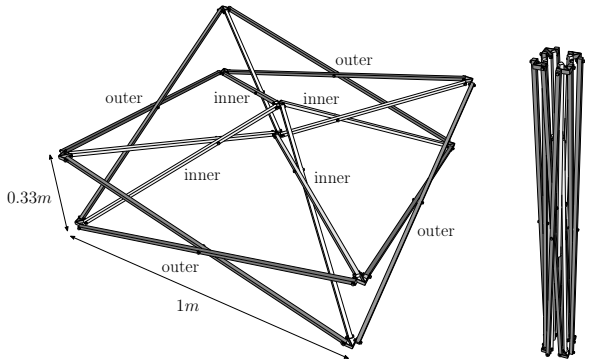

(a) deployed **(b)** folded

Figure 1: A single flat bistable module with outer and inner SLEs indicated.

(A-B). The maximum folding load is reached at point B (referred to as peak load in the sequel of the paper), followed by a snap-through from B to D. The required load becomes negative (i.e. changes direction) from C to E. This implies that without this restraining force, the structure would 'snap' to point E in a dynamic fashion. After point D (referred to as minimum load in the sequel), the bent beams gradually become straight again and internal stresses relax. Point E can be considered as the final folded configuration. When the structure is subjected to gravity, the load-displacement curve shifts upwards for this particular structure, because the folding force acts against gravity resulting in a higher required load for transformation. When the shift due to self-weight becomes too large, the curve has no negative part any more which implies that the structure would have the tendency to unfold by itself from the folded state to the deployed configuration, provided that it can overcome the geometric incompatibility. (Fig. 2). In all subsequent simulations i.e. in transformation analyses as well as in analyses of the deployed structure, gravity is considered. When finite joint dimensions are taken into account, the maximum folding load increases [18]. Technically, finite size joints are always present in scissor structures and are included in all the simulations as is explained in Section 2.2. Frictional effects unavoidably occur in real life structures and mechanisms, resulting in an increase of the transformation forces, but are not considered in this contribution for the sake of simplicity and computational efficiency.

The following opposing trends are observed in the nonlinear transformation problem, which makes its solution non-trivial:

1. Point D must be negative in load to maintain a structural snap-through with C-E being a negative branch. The position of point D is related to the bending stiffness of the inner SLE's and to the self-weight. The bending stiffness can be increased to shift point D down by choosing different materials or by increasing the corresponding cross sectional dimensions. Larger cross sectional dimensions or a denser material result in a heavier structure, with a larger self-weight shifting point D upwards.
2. In order to facilitate the deployment, it is desirable that the peak load at point B is be as low as possible, which is related to the bending stiffness of the inner SLE's. A lower peak load can be reached by lowering the stiffness of the inner SLE's.
3. The initial gradient at A (also related to the bending stiffness of the inner SLE's) is representative for the structural stiffness in the deployed state. Increasing the bending stiffness of the inner SLE's results in increasing the stiffness of the structure in the deployed state. A higher stiffness of the structure in the deployed state is beneficial for the service state, however, it potentially decreases the safety of the deployment due to the increased energy release during transformation, i.e. the snap-through becomes more difficult to control.

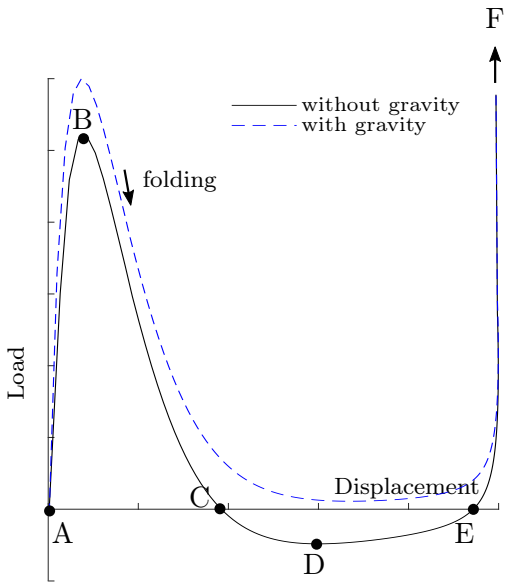

Figure 2: The load required for transformation as a function of the vertical displacement between the center points. If the self-weight is to high i.e. there is no negative part of the curve, spontaneous unfolding of the structure happens.

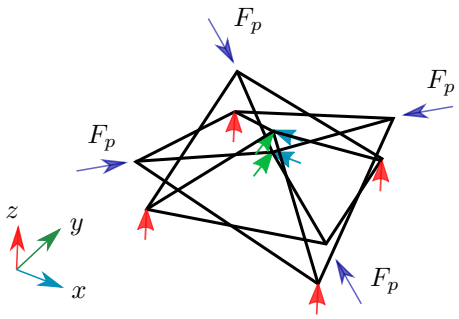

Figure 3: Applied loads F_p and boundary conditions for a single module.

2.2. Design variables

In this example, the overall dimensions of the deployed module are considered as fixed i.e. its length L (1 m) and height H (0.33 m). Hollow rectangular cross sections are chosen to obtain a lightweight structure and because the beam-to-beam connections are simpler from a technological point of view than for circular cross sections. The height h of the upper centre point (CT in Fig. 4) and the cross-sectional dimensions are geometric variables in the optimisation process while the height z of the lower centre point (CB in Fig. 4) and the hub size R are dependent variables (the connection of several beams is ensured through hubs, as shown in Fig. 7). The dependent variables are calculated as follows:

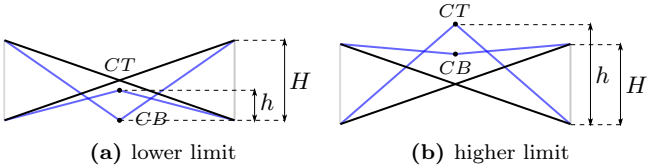

(a) lower limit **(b)** higher limit

Figure 4: Side view of the bistable scissor module (outer SLE's in black, inner SLE's in blue) with the boundary values for h/H.

1. To determine the height (z in Fig. 5) of the lower centre point CB, the following calculation is used: The length $l = b + d$ is:

$$l = \sqrt{h^2 + (D - 2R)^2} \tag{1}$$

with $D = L/\sqrt{2}$ the length of a diagonal of the square module. The half-length of a beam in an outer SLE (e in Fig. 5) is:

$$e = \frac{\sqrt{H^2 + (L - 2R)^2}}{2} \tag{2}$$

The spacing between two joints connecting the outer SLE's, ensuring compatibility of the module in the folded configuration (v in Fig. 6), is given by:

$$v = 2\sqrt{2}R - 2R \tag{3}$$

The ratio $x = \frac{d}{l}$ is:

$$x = \frac{(L - 2R)^2 - v^2}{2\sqrt{4e^2 - v^2}l - 2hH} \tag{4}$$

The height of the lower centre point z, is given by:

$$z = h - \frac{1 - x}{x}H \tag{5}$$

2. The hub size changes according to the cross sections of the beams to allow their sound connection to the hub. The hub dimensions depend on the dimensions of the cross sections of the beams and the spacing in between the beams of an SLE (Fig. 7). By varying the cross sectional dimensions of the beams, this hub size (as well as the distance between the beam axes in the model) will change and the geometry of the module is consequently adapted. The hub size R is given by:

$$R = \max(r_i, r_o) \tag{6}$$

$$r_i = \frac{h_{ci}}{2} + w_{ci} + \frac{1 + \sqrt{2}}{2}s \tag{7}$$

$$r_o = \frac{h_{co}}{2} + w_{co} + \frac{1 + \sqrt{2}}{2}s \tag{8}$$

with R the hub size, r_i and r_o the minimum required size for the hub according to the dimensions of respectively the inner and outer beam cross sections, h_{ci} and h_{co} the height of the inner and outer beams, w_{ci} and w_{co} the width of the inner and outer beams and s the spacing in between the beams of an SLE, chosen to be 1 cm (Fig. 7 and Fig. 8).

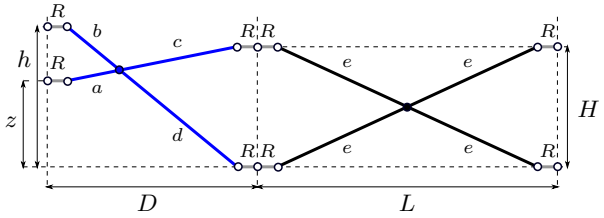

Figure 5: The inner and outer SLE's of a square polygonal module in the deployed configuration.

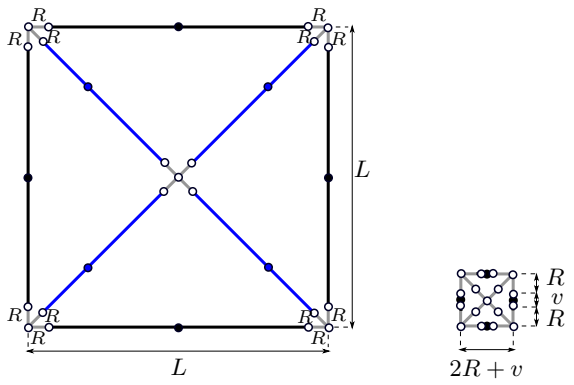

(a) deployed **(b)** folded

Figure 6: Top view of the deployed and folded square module.

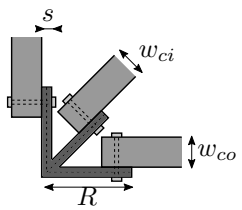

Figure 7: A corner hub connecting two outer beams and one inner beam.

In total, seven *continuous design variables* are defined:

1. The width w_{ci} of the inner SLE's.
2. The height h_{ci} of the inner SLE's.
3. The thickness t_{ci} of the inner SLE's.
4. The width w_{co} of the outer SLE's.
5. The height h_{co} of the outer SLE's.
6. The thickness t_{co} of the outer SLE's.
7. A geometrical parameter being the height h of the module in the centre relative to the height H of the module at the corners in the deployed configuration (Fig. 4).

It is worth mentioning that the cross section choices are in reality categorical design variables [38], but for simplicity they are treated as continuous design variables in this contribution.

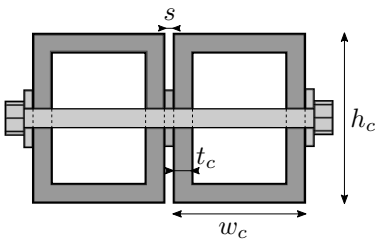

Figure 8: Cut view of an SLE hinge showing the width, height and thickness of the beams.

The lower and upper bounds for the width and the height of the cross sections are chosen to be 1/100 and 1/20 of the beam lengths, respectively. The thickness of the cross section is chosen to be between 2 mm and 5 mm, which corresponds to 1/2 of the lower limit for the width and the height of the cross section. The lower limit for h/H is chosen in a way that the lower centre point CB can never be located below the lower corner points (Fig. 4a), while the upper limit is chosen in a way that the structure can be folded using horizontal forces in the corner points (Fig. 4b). A higher h/H would imply that the vertical position of the lower centre point CB is higher than the vertical position of the upper corner points (equal to H) in the deployed configuration. For the structure to fold, it is necessary that point CB goes downwards during the folding process. This could be achieved by an additional vertical force in one of the centre points.

	Lower limit	Upper limit
w_{ci} [cm]	1	5
h_{ci} [cm]	1	5
t_{ci} [mm]	2	5
w_{co} [cm]	1	5
h_{co} [cm]	1	5
t_{co} [mm]	2	5
h/H	0.4	1.3

Table 1: Lower and upper bounds for the geometric design variables.

Additionally, different material pairs for the beams are considered, since this is relevant to adjust the SLE stiffness. Three cases have been investigated:

1. Aluminium is used for all the beams.
2. Aluminium is used for the outer SLE's while HDPE (high-density polyethylene) is used for the inner SLE's (as in [21]).
3. HDPE is used for all the beams.

The material parameters are given in Table 2. The material pairs are not design variables. They are considered separately and their results are critically compared.

	HDPE	Aluminium
Young's modulus	0.8 GPa	70 GPa
Poisson's ratio	0.4	0.35
Density	940 kg/m^3	2700 kg/m^3
Yield strength	31.7 MPa	200 MPa

Table 2: Material parameters of HDPE and aluminium.

2.3. Objectives

The two objectives of the structural optimisation in this contribution are to keep as low as possible the maximum load required for folding/deployment, as well as the deflection of the structure in the deployed configuration under structural constraints δ (listed in Section 2.4):

1. The maximum load required for deployment is deduced from the load-displacement curve which is obtained from the computational analysis of the transformation phase (using FEM) and corresponds thus to point B on the load-displacement curve discretized into load increments in the computations $[1, n_{inc}]$ in Fig. 2. The maximum load can be given by:

$$\max_{i\in[1,n_{inc}]} \left(\sum_{p=1}^{n_{forces}} F_{p,i} \right) \tag{9}$$

with n_{inc} and n_{forces} the number of increments and forces respectively.

2. The the maximum deflection under self-weight in the deployed configuration is obtained from a FE analysis in the service state (i.e. maximal vertical displacement of the FE nodes). No other service loads have been applied. The maximum deflection is given as:

$$\max_{j\in[1,n_{nodes}]} (\delta_j) \tag{10}$$

with n_{nodes} the number of nodes in the structure. For the deployed structure, the boundary conditions are the same as during transformation. These are described in Section 4 for the single module and in Section 5 for the multi-module structure.

2.4. Constraints

The following *constraints* are considered in the multi-objective optimisation problem:

1. The maximum von Mises stress $\sigma_{vonMises}$ during deployment and in the deployed configuration, obtained from the FE simulations, is below the yield stress σ_y of the material.

$$\max_{i\in[1,n_{inc}]}\left(\max_{k\in[1,n_{el}]}(\sigma_{vonMises,i,k})\right) < \sigma_y \qquad (11)$$

with n_{inc} and n_{el} the number of increments of the simulations and finite elements respectively.

2. The maximum deflection in the deployed configuration, obtained from the FE simulation of the deployed state, is chosen to be $L/100$ with L the maximum spatial dimension of the structure i.e. 1 m in the case of a single module. This constraint is less strict than for traditional structures [35].

$$\max_{j\in[1,n_{nodes}]}(\delta_j) \leq \frac{L}{100} \qquad (12)$$

with n_{nodes} the number of nodes.

3. Buckling of the beams must be avoided in the deployed configuration. An analytical calculation is implemented for each beam following Eurocode 9 [32, 33, 35]. The critical buckling load is:

$$P_{cr} = \pi^2 \frac{EI}{L^2} \qquad (13)$$

with E the Young's modulus, L the longest semi-length of the beam and I the moment of inertia in case of in-plane buckling and L the length of the whole beam and I the sum of the moments of inertia of both beams in case of out-of-plane buckling, as derived by Koumar et al. [35]. Only compression forces are taken into account in this contribution. Eq. (13) is used to calculate the design buckling resistance N_{Rd} following Eurocode 9 [32]. Since hollow cross sections are used, members are not prone to torsional deformations and only flexural buckling (caused by bending in a member in compression) was checked. Since there is always axial compression as well as bending, flexural buckling is verified as follows:

$$\left(\frac{\max_{i\in[1,n_{inc}]}\left(\max_{k\in[1,n_{el}]}(N_{Ed,i,k})\right)}{\chi_{min}\omega_x N_{Rd}}\right)^{\psi_c} + \frac{1}{\omega_0}\left[\left(\frac{\max_{i\in[1,n_{inc}]}\left(\max_{k\in[1,n_{el}]}(M_{y,Ed,i,k})\right)}{M_{y,Rd}}\right)^{1.7} + \left(\frac{\max_{i\in[1,n_{inc}]}\left(\max_{k\in[1,n_{el}]}(M_{z,Ed,i,k})\right)}{M_{z,Rd}}\right)^{1.7}\right]^{0.6} \leq 1.0 \qquad (14)$$

with N_{Ed}, $M_{y,Ed}$, $M_{z,Ed}$ the compression force and the bending moments obtained from the FE simulations, ψ_c, ω_x, ω_0 values taken from Eurocode 9 [32], N_{Rd} the design buckling resistance and $M_{y,Rd}$, $M_{z,Rd}$ the bending moment capacities calculated following Eurocode 9 [32].

4. The minimum load F_{min} during the folding process has to be negative (C-E on Fig. 2), to counteract gravity induced deployment from the folded configuration [18].

$$\min_{i\in[1,n_{inc}]}\left(\sum_{p=1}^{n_{forces}} F_{p,i}\right) < 0 \qquad (15)$$

with n_{forces} the number of applied forces.

3. Formulation of the optimisation problem

To find optimal solutions which combine a low peak force during transformation with a low deflection under self-weight in the deployed configuration, the optimisation problem given in the box below (Eq. (16)) has to be solved.

s_l refers to the design variables: the cross sectional dimensions for 2 groups of cross sections ($\boldsymbol{s} = (w_{ci}, h_{ci}, t_{ci}, w_{co}, h_{co}, t_{co})$) and the geometrical parameter h/H, S_l are the intervals of s_l. The applied force F_p, the stress $\sigma_{vonMises}$ and the section forces N_{Ed} and M_{Ed} all depend on the design variables s_l. Their dependency on the design variables is non-linear and they are sampled point-wise at each increment of the non-linear FE simulations of transformation for each set of $\boldsymbol{s}$.

The optimisation approach is based on the NSGA-II [39], which is a popular method for multi-objective optimisation problems in civil engineering [34, 35, 40]. An initial population N of 100 individuals is chosen randomly. Each individual is associated a different design parameter set, which means that the individuals consist of the values of the design variables. The parent P_t and offspring Q_t population both have N members. The combined population $R_t = P_t \cup Q_t$ is sorted according to nondomination levels L_1, L_2... An individual is part of a nondomination level L_n if no other individual exists within L_n which has a lower value for all the objectives. The nondomination levels are selected starting from L_1 until its size is equal to N. From the last accepted level, individuals are chosen that are located in a region with the smallest number of points using the crowding-distance principle, to maintain a good spread of solutions. A new offspring population is created by applying the usual crossover and mutation operators by randomly picking parents from P_{t+1}. Crossover is the procedure of combining genes of the parents. The probability of crossover P_{ci} used in this contribution is 0.9. Simulated Binary Crossover is used, in which the gene values of the children have the same distance from the average gene value of the parents. In the mutation phase, the characteristics of the individuals are changed. The probability

$$\underset{\boldsymbol{s}}{\text{minimize}} \quad \left\{ \max_{i\in[1,n_{inc}]} \left(\sum_{p=1}^{n_{forces}} F_{p,i}\left(\boldsymbol{s}\right) \right); \right. \tag{16a}$$

$$\left. \max_{j\in[1,n_{nodes}]} \left(\delta_j\left(\boldsymbol{s}\right)\right) \right\} \tag{16b}$$

$$\text{subject to} \quad \max_{i\in[1,n_{inc}]} \left(\max_{k\in[1,n_{el}]} \left(\sigma_{vonMises,i,k}\left(\boldsymbol{s}\right)\right) \right) < \sigma_y \tag{16c}$$

$$\max_{j\in[1,n_{nodes}]} \left(\delta_j\left(\boldsymbol{s}\right)\right) \leq \frac{L}{100} \tag{16d}$$

$$\left(\frac{\max\limits_{i\in[1,n_{inc}]} \left(\max\limits_{k\in[1,n_{el}]} \left(N_{Ed,i,k}\left(\boldsymbol{s}\right)\right) \right)}{\chi_{min}\omega_x N_{Rd}\left(\boldsymbol{s}\right)} \right)^{\psi_c} + \frac{1}{\omega_0} \left[\left(\frac{\max\limits_{i\in[1,n_{inc}]} \left(\max\limits_{k\in[1,n_{el}]} \left(M_{y,Ed,i,k}\left(\boldsymbol{s}\right)\right) \right)}{M_{y,Rd}\left(\boldsymbol{s}\right)} \right)^{1.7} + \left(\frac{\max\limits_{i\in[1,n_{inc}]} \left(\max\limits_{k\in[1,n_{el}]} \left(M_{z,Ed,i,k}\left(\boldsymbol{s}\right)\right) \right)}{M_{z,Rd}\left(\boldsymbol{s}\right)} \right)^{1.7} \right]^{0.6} \leq 1.0 \tag{16e}$$

$$\min_{i\in[1,n_{inc}]} \left(\sum_{p=1}^{n_{forces}} F_{p,i}\left(\boldsymbol{s}\right) \right) < 0 \tag{16f}$$

$$\text{with} \quad s_l \in S_l \qquad l = 1, ..., 7 \tag{16g}$$

of mutation P_{mi} is chosen to be 0.1. This procedure of creating a new generation is repeated until the result is converged (i.e. a smooth Pareto front is obtained which doesn't change for several generations) or until the defined maximum number of generations is reached (set to be 200).

3.1. Computational implementation

First, the NSGA-II algorithm (written in Matlab [39]) generates the initial population and sends the design variables for each individual to Grasshopper (a plug-in for Rhinoceros [41]), in which the geometry is updated parametrically (i.e. the height of the centre points, the spacing in between the beams and the hub size) and the input files are written for Abaqus FE simulations [42].

In the structural FE model, which is described in detail in [18], the semi-length of each beam (between the hub and the pivotal connection) is modelled as four Timoshenko beam elements, which has been verified to correspond to a converged mesh. The connections are simulated with the geometrically nonlinear connector type 'hinge', incorporating the update of the hinge orientation during transformation. In reality, the two beams in an SLE do not lie in the same plane. This is taken into account by incorporating a spacing between the beam elements. This finite spacing between the beams promotes the beams of the inner SLE's to buckle out-of-plane for large height-to-width ratios. The hub is described by a stiff grid of small beam elements, as in [11].

Two FE computations are performed for each design: 1) a linear analysis of the structure in the deployed state to measure the maximum deflection under self-weight and 2) a non-linear analysis of the folding from the deployed configuration without considering friction in the hinges. To solve the snap-through problem, the modified Riks solution strategy is used [18]. The complex non-linear simulations make the optimisation of bistable scissor structures time-consuming. To reduce the computational time, the simulations of different individuals in the same population are run in parallel.

The output of these sets of FE simulations is accessed using a Python script and the constraints are calculated. The objectives and constraints are sent back to Matlab in which the NSGA-II algorithm evaluates the objective functions and creates a new population.

4. Optimisation of a single module

This section focuses on a square flat polygonal module (Fig. 1) with boundary conditions shown in Fig. 3. The center points are constrained to move only in the vertical direction z. The folding force used in the objective func-

tion is the arithmetic sum of the 4 applied diagonal corner forces ($4.F$).

The evolution of the Pareto front throughout the optimisation process of the pure HDPE case is given in Fig. 9. Because of the many constraints and the limited range for the design variables, it took in this case more than 50 generations to find solutions to the problem. Once a few solutions are found, the Pareto front evolved in around 100 generations towards the converged Pareto front.

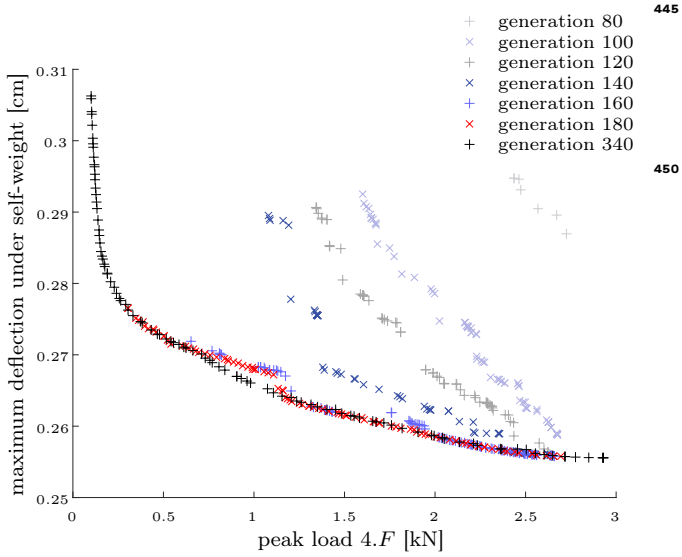

Figure 9: Evolution of the Pareto front throughout the optimisation process.

Generation 180 in Fig. 9 corresponds to a stable Pareto front, even though it is not smooth. The smoothness can be recovered by decreasing the allowed maximum arc increment in the FE simulations to approximate the peak load more accurately. This of course results in a longer computational time for a simulation, which is why it was attempted systematically only for a close to converged generation. In the discussed case more than 200 generations were needed to reach a smooth Pareto front (generation 340 in Fig. 9). Runs with different sets of optimisation parameters have been carried out for the same structure. The results were comparable, meaning that a stable solution is reached and that the optimisation methodology is robust and applicable for complex problems.

The final Pareto fronts obtained for the 3 material pairs (pure Al; Al-HDPE; pure HDPE) are given in Fig. 10 with the corresponding design variables for points A, B and C shown in Table 3. The case in which HDPE was used for all the beams is quite different from the other scenarios. The deflection in the deployed configuration (2.6 mm to 3.1 mm) is clearly higher for the same peak load as for the other cases (0.39 mm to 1.6 mm for aluminium and HDPE combined, 0.4 mm to 1.3 mm for pure aluminium), resulting in more compliant structures, as expected. When comparing the pure aluminium case to Al-HDPE, a decrease in the peak load can be observed for the same deflection for the composite structure. This difference in peak load decreases for low deflections (high peak load regime) and increases for large deflections (low peak load regime). The lowest peak load observed for the pure Al structure is 0.521 kN, while the lowest peak load for Al-HDPE is almost 5 times lower, 0.101 kN (corresponding to 4 diagonal point loads of 25.25 N applied at every corner of the module). Since low peak loads are desired, the Al-HDPE case corresponds to more optimal structures. Moreover, for the Al-HDPE structure, the weight ranges from 3 to 4 kg, which is less than the 4 to 6 kg for the pure Al structure, and somewhat more than the 2 to 3 kg for the pure HDPE structure. The composite structure thus seems to be a good compromise, joining low weight and high stiffness in the deployed configuration (comparable to pure Al) with a possibility of reaching low peak forces (comparable to pure HDPE).

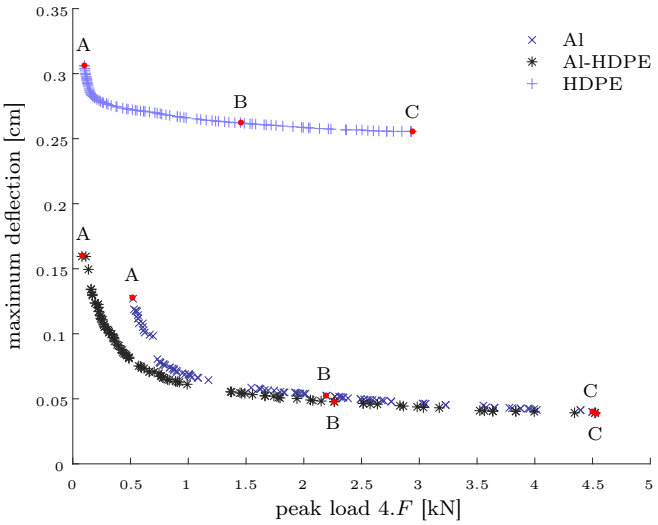

Figure 10: Comparison of the Pareto fronts for structures built from different material pairs.

In Fig. 11, the normalised values (relative to the lower and upper bounds) of the design variables on the Pareto sets are shown. This graphical representation is interesting because it shows whether the lower or upper limits of the design variables are reached and whether the optimal solutions are well-spread or rather focused around a certain value.

For the pure Al structure, the outer beams have the lowest width while the inner beams have the largest width and height (Fig. 11a). This can be explained by higher stresses observed in the *inner beams* (for the sake of briefness stress plots are not included for single modules here). The solution with the lowest peak force (solution A on Fig. 10) corresponds to a structure in which the cross section of the outer beams is small (reaching the lower bound for the width and height). The solution with the highest peak force (solution C on Fig. 10) corresponds to a structure in which the cross section of the outer beams is thin and high. The smaller the cross section of the outer beams, the lower their self weight is, leading to a

		A	B	C
Al	outer beams			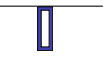
	inner beams			
	geometry			
Al-HDPE	outer beams			
	inner beams			
	geometry			
HDPE	outer beams			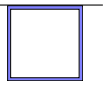
	inner beams			
	geometry			

Table 3: Beam cross sections for the solutions A, B and C on the Pareto fronts in Fig. 10.

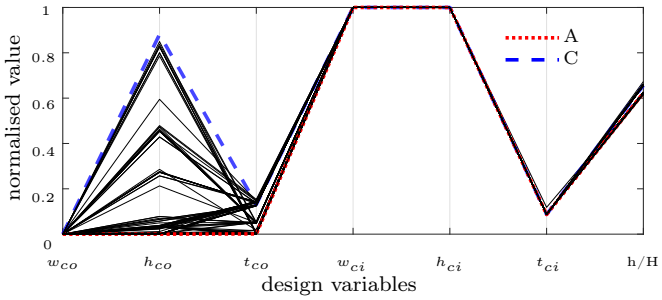

(a) aluminium for all the beams

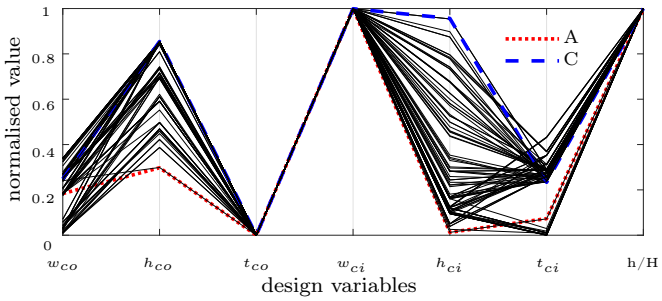

(b) aluminium for the outer SLE's, HDPE for the inner SLE's

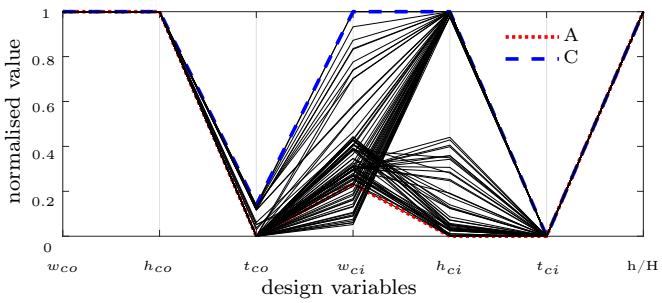

(c) HDPE for all the beams

Figure 11: Comparison of the Pareto sets. The normalised values (relative to the lower and upper bounds) are given for each design variable (the width, height and thickness of the outer SLE's w_{co}, h_{co} and t_{co}, the width, height and thickness of the inner SLE's w_{ci}, h_{ci} and t_{ci} and the geometric variable h/H).

smaller deflection. Smaller inner cross sections also lead to an easier deployment and thus a lower peak load. The most compliant and stiffest designs in this paper, i.e. with the highest and the lowest deflections under self weight in the deployed configuration are denoted as A and C systematically throughout this contribution, with case B an intermediate optimum solution between A and C.

In the pure HDPE case, the outer beams have the largest width and height and the inner beams are thin (Fig. 11c), which is the opposite trend of the observations made in the pure Al case. For pure HDPE, the *outer beams* were observed to have the higher stresses which explains this opposite trend. Solution A on Fig. 10 for pure HDPE corresponds to a structure in which the cross section of the inner beams reaches the lower bound for the width and height. Solution C on Fig. 10 corresponds to a structure in which the cross section of the inner beams reaches the upper bound for the width and height. The inner beams determine the compliance of the structure by limiting the deflection caused by the weight of the beams which means that the larger the inner beams, the smaller the deflection.

In the composite Al-HDPE structure, the width of the HDPE beams reaches the upper bound (Fig. 11b). Solution A on Fig. 10 corresponds to a structure in which the cross section of the outer beams is as small as possible while the cross sections of the inner beams have a large width and a small height. These wide and low cross sections for the inner beams allow for in-plane bending, leading to an easier transformation and thus a lower peak force. Solution C on Fig. 10 corresponds to a structure in which the cross section of the outer beams reaches the lower bound for the width and the higher bound for the height and the cross section of the inner beams is as large as possible (Table 3). These large cross sections for the inner beams decrease their tendency to bend during transformation, leading to a higher peak force but also to a higher stiffness in the deployed state. As was the case for pure HDPE, the inner beams determine the compliance by limiting the deflection caused by the weight of the beams. The cross section difference between the inner and the outer beams can be explained by the different elastic moduli of the materials. Solution B on Fig. 10 is always following the trends set between A and C for all material pairs.

For pure HDPE and for Al-HDPE cases, the optimal structural geometry is the one in which the upper centre point is as high as possible, which seems to be a dominating requirement. This results in the largest geometric incompatibilities, leading to a stiffer structure in the de-

ployed state but also to a higher peak load. When only aluminium is used, the bending of the inner beams, which is a result of the geometric incompatibilities, is more difficult due to a higher material stiffness, leading to larger peak forces. This leads to optimized structures having a lower upper centre point.

In Fig. 12, the values of the constraints are given for each solution. When all of the values for a constraint for all of the solutions on the Pareto front are close to the upper bound, this constraint is identified as a governing constraint for this specific optimisation problem. The yield stresses and the buckling constraints are always satisfied in the simulations yielding solutions far from the boundary (except for the outer beams in the pure Al case). On the contrary, the minimum load and the maximum displacement constraints are more critical in all cases. The minimum load constraint is critical in all cases. This is due to the structural behaviour of these flat modules in general, in which the magnitude of the peak load (point B in Fig. 2) is found to be always higher than the magnitude of the minimum load (point D in Fig. 2), based on observations [18]. Consequently, as the peak load is minimised, the minimum load converges towards values closer to zero. It is noteworthy that the choice of the design bounds imposed in the optimisation process is crucial (several of the solutions operate on these bounds, as shown in Fig. 11).

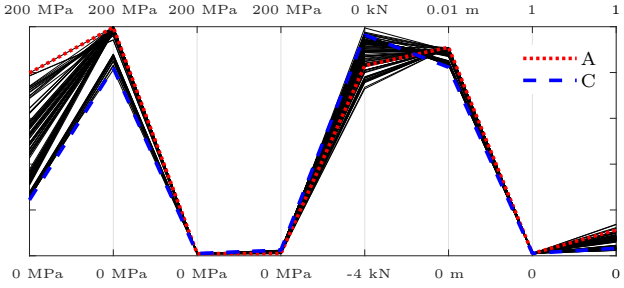

(a) aluminium for all the beams

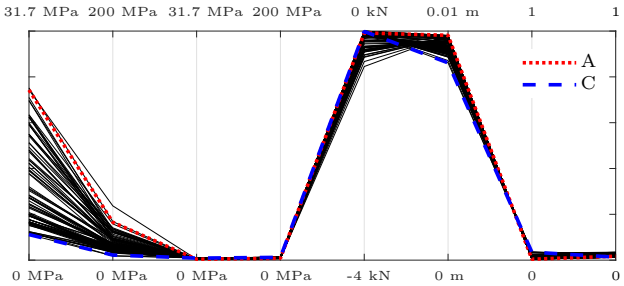

(b) aluminium for the outer SLE's, HDPE for the inner SLE's

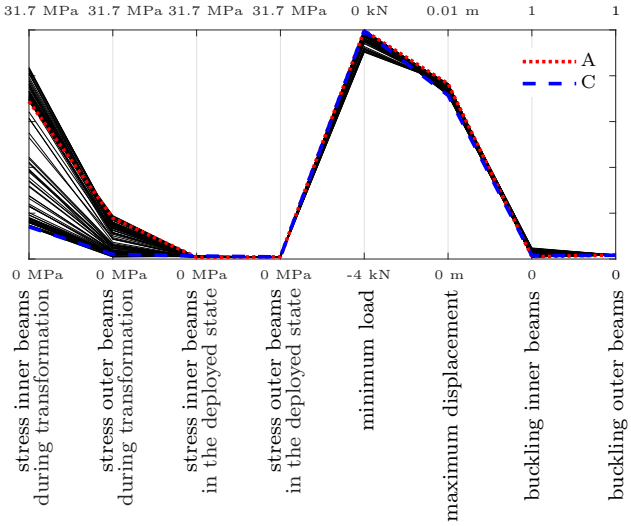

(c) HDPE for all the beams

Figure 12: Comparison of the constraints for the 3 cases.

5. Optimisation of multi-module structures

A flat roof with a span of 5 m composed of 5 by 5 modules is now considered as multi-module structure. One of the main goals here is to investigate whether the results obtained for a single module remain applicable for multi-module structures when different boundary conditions are applied to the structure. Two sets of boundary conditions are considered: a vertical planar support that mimics BC of Section 4 and rail supports along 2 sides. The objective functions, design variables and constraints are the same as in Section 4. The maximum deflection in the case of the flat roof becomes 5 cm. HDPE was used for the inner SLE's and aluminium for the outer SLE's using the material parameters of Table 2 and design bounds of Table 1.

5.1. Lower plane vertical support boundary conditions

Here, the roof has been optimised with comparable boundary conditions and loads as for the single module. This set of boundary conditions of course does not match a practical application, but is used for comparison with the single module. Therefore it is expected to yield similar results. Internal lower nodes are restricted against vertical displacement in the z-direction. Edge lower nodes are restricted against vertical displacement in the z-direction and horizontal displacement in x or y (different for each edge). Edge upper nodes are restricted against horizontal displacement in x or y (different for each edge). Forces are applied at the upper points of the other two sides of the structure (Fig. 13a). The same boundary conditions apply for the transformation as well as for the deployed structure under self-weight. The folding force used in the objective function is the arithmetic sum of all of the applied forces and of the horizontal reaction forces along the two constrained edges (11.F).

The resulting Pareto front is shown in Fig. 14 together with the Pareto front of the composite Al-HDPE single module of Section 4. The maximum deflection of the multi-module structure under self-weight is smaller because the horizontal movement of the outer nodes of the modules is restricted at two edges of the structure (that is a minor difference in BC with respect to the single module case). The peak force is higher for the multi-module structure since more beams have to bend to transform the structure.

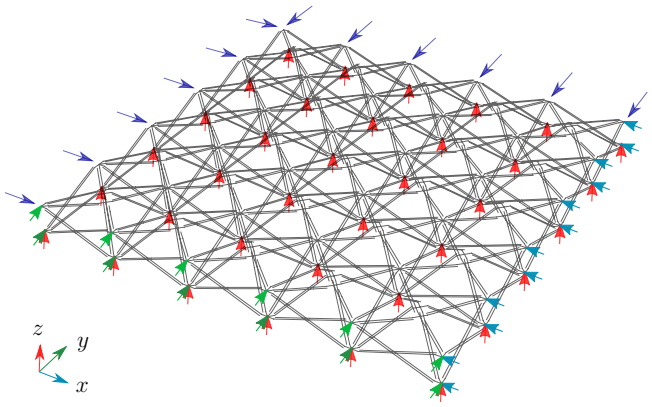

(a) boundary conditions and loads

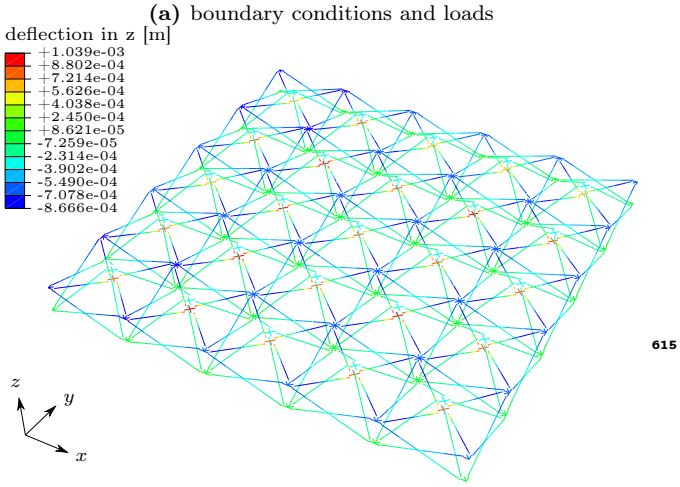

(b) deformed shape in the deployed configuration

Figure 13: Comparable boundary conditions and loads as for the single module.

The solution with the lowest deflection and the highest peak force has a high peak force of 35.3 kN and a deflection of only 0.02 cm (point C on Fig. 14), while the solution with the lowest peak load and the highest deflection has a peak load of 0.88 kN and a deflection of 0.10 cm (point A on Fig. 14).

It is interesting to notice that, although the majority of solutions of the optimisation of the multi-module structure has a higher peak load and lower deflection than the solutions for the single module, there is a domain in which similar peak loads for a given maximum deflection appear. However, it has to be emphasised that the values of the design variables of overlapping points in Fig. 14 are not the same for the single and multi-module solutions. While point C* on the Pareto front of the single module is a structure with outer beams of 18x44x2 mm and inner beams of 50x48x3 mm, the closest point on the Pareto front of the multi-module structure has much thinner outer beams of 17x25x2 mm and inner beams of 50x20x3 mm (for the same peak load of 4.5 kN and maximum deflection of 0.039 cm).

Examining Pareto sets gives valuable complementary information (Fig. 15). The same trends can be observed for

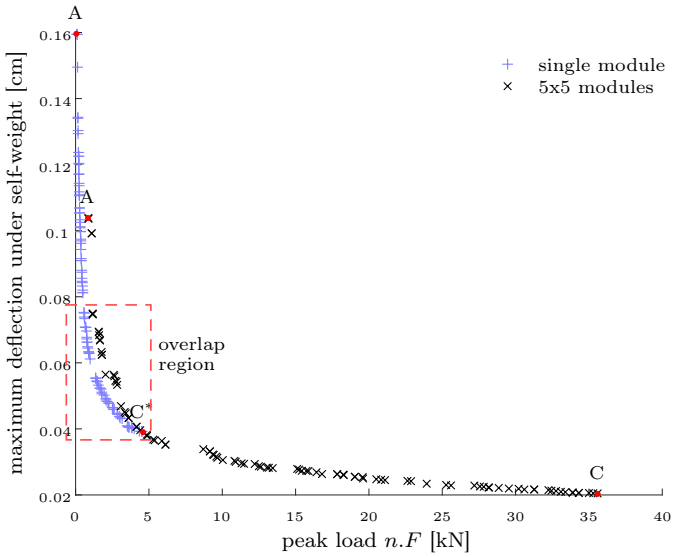

Figure 14: Comparison of the Pareto fronts for the single module and the flat structure consisting of 5 by 5 modules.

the solutions for the single module and the multi-module structure. The thickness of the aluminium beams is as low as possible while the width of the HDPE beams is as high as possible. The optimal structural geometry is the one in which the upper centre point is as high as possible, which results in the largest geometric incompatibilities, leading to a stiffer structure in the deployed state but also to a higher peak load. Since the Pareto sets are almost identical, it can be concluded that the optimisation of a multi-module structure *can* be deduced from the optimisation of a single module, *provided that the boundary conditions and the applied loads are comparable.*

In Fig. 16, the load-displacement curves are plotted for the solutions denoted A and C, and for the solution of the multi-module structure closest to solution C* of the single module. The displacement is the relative vertical displacement between the center points of a module taking the deployed configuration as reference. This is done for all subsequent plots for multi-module structures. The load-displacement curves for the solutions with the highest deflection (solutions A) have a very low peak load, a snap-through that is not very pronounced (the difference between the peak load and the minimum load is rather small), and the minimum load is close to zero. For the solutions with the lowest deflection (solutions C), a high peak load can be observed with a higher snap-through magnitude and a more negative minimum load. The solutions for the single module follow the same trend as the multi-module solutions i.e. the snap-through occurs around the same displacements, the main difference being a higher required load for transformation for the multi-module structure. There is a minor difference in the displacement for the closed configurations between the solutions with the highest peak load and the lowest peak load due to different member lengths, resulting from different hub sizes required to accommodate different cross sections.

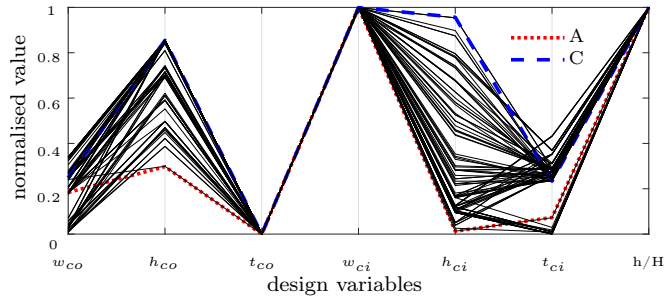

(a) single module

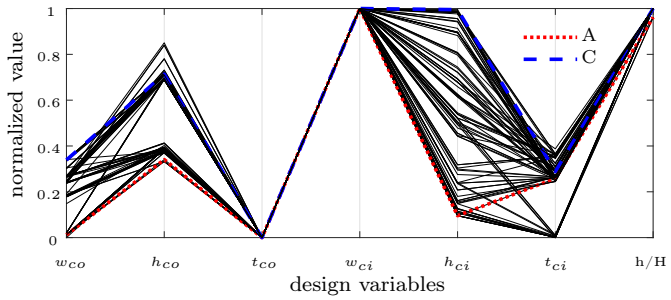

(b) 5x5 modules

Figure 15: Comparison of the Pareto sets for the single module and for the flat structure consisting of 5 by 5 modules.

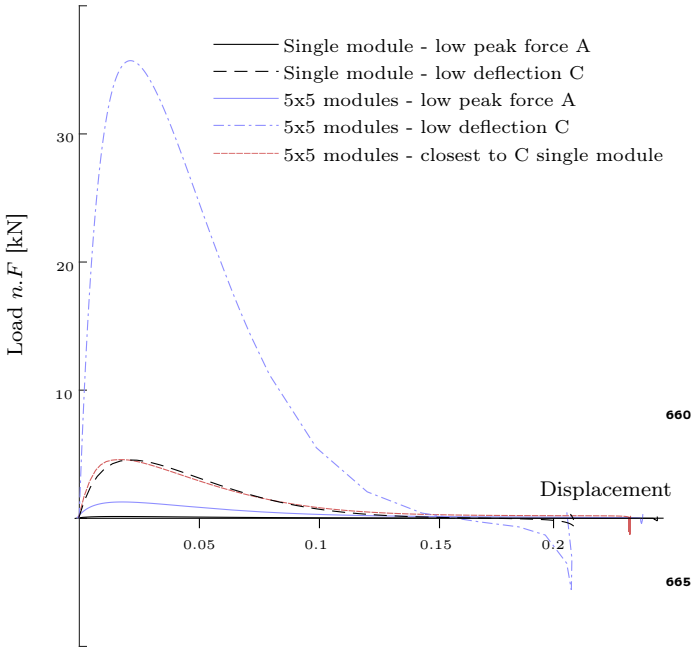

Figure 16: Comparison of the load-displacement curves for solutions A and C for the single and multi-module structure with planar support BC.

In Fig. 17, the comparison of the results and the constraints is given for the single module and the multi-module structure. The same trends for the stresses and the buckling can be observed i.e. the yield stresses and the buckling constraints are always satisfied. For the single module, the minimum load constraint and the maximum deflection constraint are both critical, while for the multi-module structure, only the minimum load constraint is found to yield solutions close to the constraint. The multi-module structure thus appears to be easier to design within the predefined bounds than a single module.

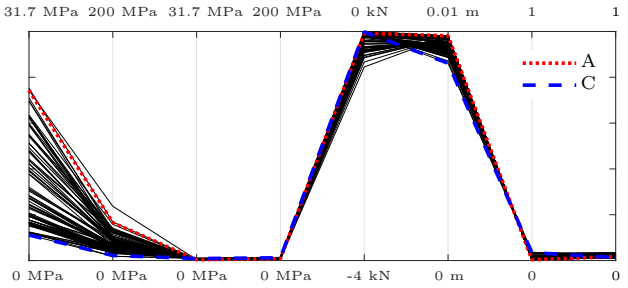

(a) single module

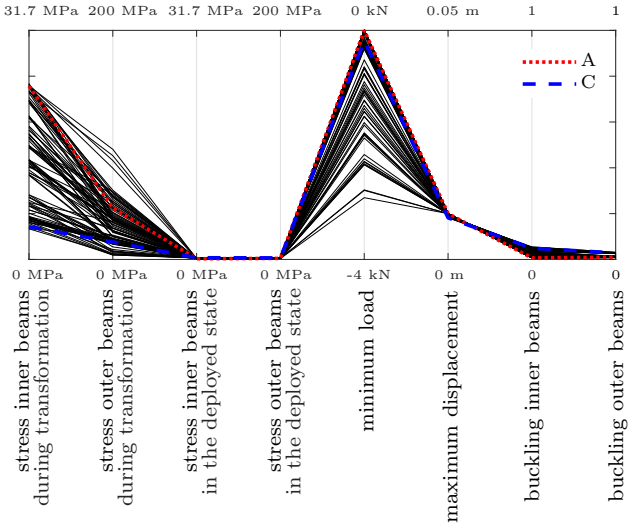

(b) 5x5 modules

Figure 17: Comparison of the values of the constraints.

5.2. Side rail supported boundary conditions

In reality, a deployable roof will not be subjected to horizontal plane support boundary conditions, therefore a more realistic set of boundary conditions that mimic the 2 bottom edges of the structure running along two horizontal, mutually perpendicular rails is adopted here. The lower corner point between the two supported sides is fixed in x, y and z. The lower points of a supported side are free to move *along the edge of the structure* in x or y and they are fixed in the vertical direction z (i.e. like moving along a rail). The upper points on constrained sides can only move in a vertical plane set along a rail (fixed in x or y). Forces are applied on the upper points of the two other sides of the structure to transform it (Fig. 18a). These BC thus constrain two sides of the structure, leaving the opposite sides and corner point free. The same boundary conditions apply for the transformation as well as for the deployed structure under self-weight. This explains the deformed shape under self weight shown in Fig. 18b.

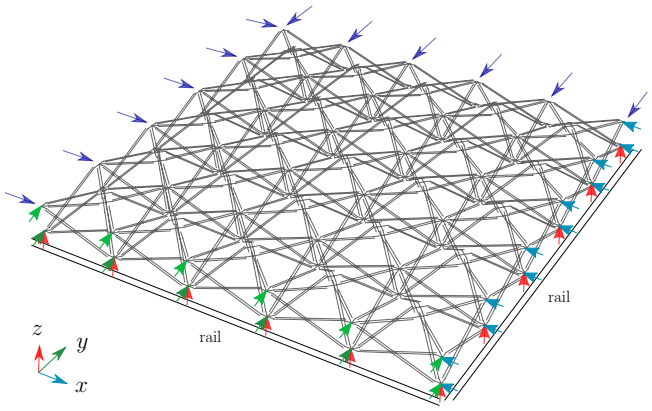

(a) boundary conditions and loads

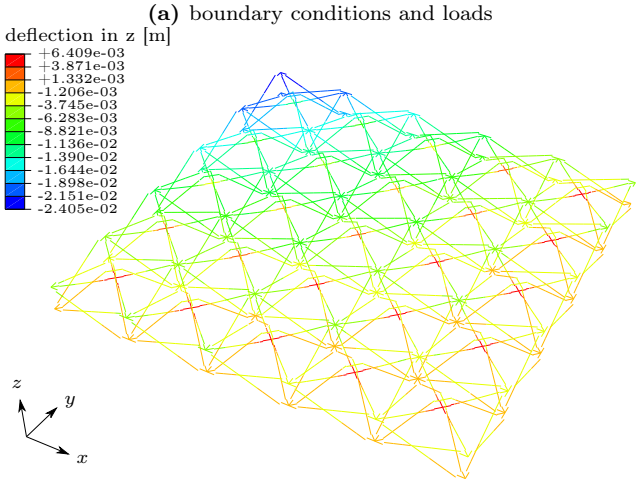

(b) deformed shape in the deployed configuration

Figure 18: Side rail boundary conditions and applied loads.

The Pareto front resulting from the optimisation is given in Fig. 19. The direct graphical comparison with Section 5.1 is not attempted due to the *large difference in Pareto fronts*. The solution with the lowest deflection and the highest peak load (C) has a deflection of 2.20 cm and a peak load of 1.648 kN (compared to a deflection of 0.02 cm and a peak load of 35.3 kN for Section 5.1). The solution with the lowest peak load and the highest deflection (A) has a peak load of only 0.662 kN and a deflection of 2.42 cm (compared to a peak load of 0.88 kN and a deflection of 0.10 cm for Section 5.1). The deflection of the roof with rail support is 20 to 100 times larger than the deflection of the roof with planar support, while the peak load is up to 30 times smaller.

The Pareto sets obtained for the two BCs are compared in Fig. 20. For planar BC (Fig. 20a), the thickness of the outer aluminium beams is as low as possible while the width of the HDPE beams is as high as possible. For rail supports (Fig. 20b), the width and height of the aluminium beams are as high as possible, while their thickness is as low as possible. The dimensions (width, height and thickness) of the inner HDPE beams are close to the lower bounds for rail supports, which is the opposite trend to the one observed for planar BC. For both cases, the optimal structural geometry is the one in which the upper centre point is as high as possible, leading to the largest geometric incompatibilities.

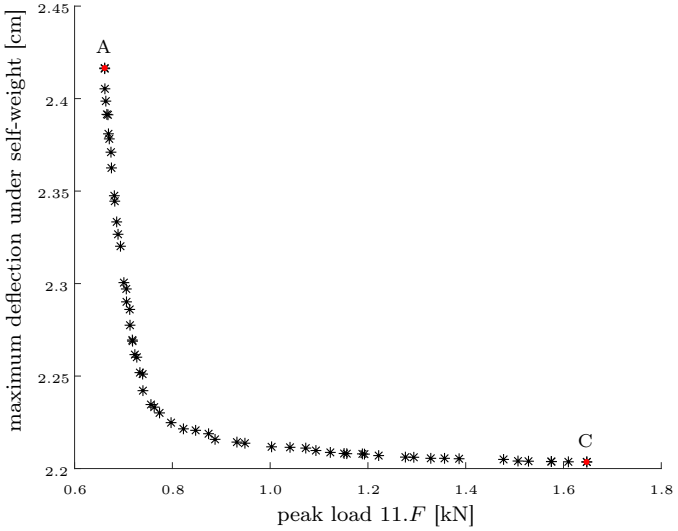

Figure 19: The Pareto front for the flat roof consisting of 5 by 5 modules with realistic boundary conditions.

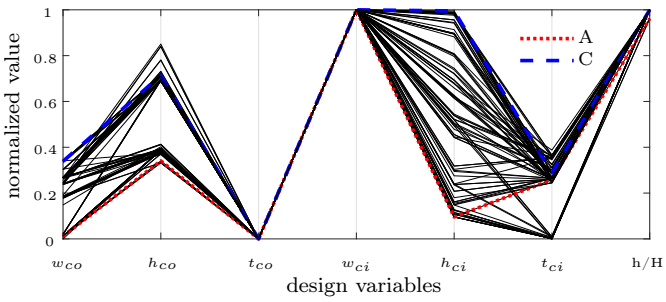

(a) comparable BCs as for 1 module

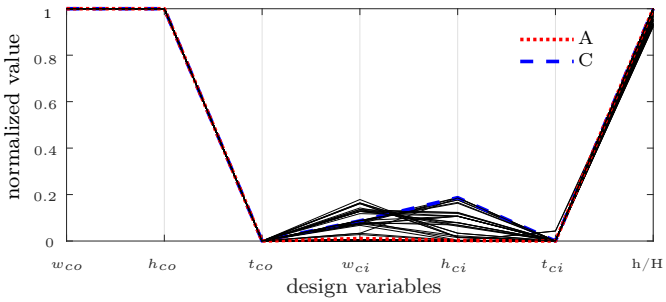

(b) realistic BCs

Figure 20: Comparison of the Pareto sets for the flat structures consisting of 5 by 5 modules.

In Fig. 21, the comparison of the results and the constraints is given. For the roof with side rail supports, the stresses are low compared to the planar support. For both cases, the buckling constraint is far from the threshold. For the side rail supports, the governing constraint is clearly the minimum load, which is very close to zero.

The significant difference in the results can be explained when looking at the stress distribution when con-

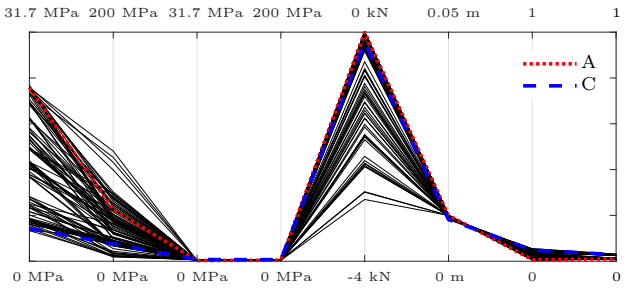

(a) comparable BCs as for 1 module

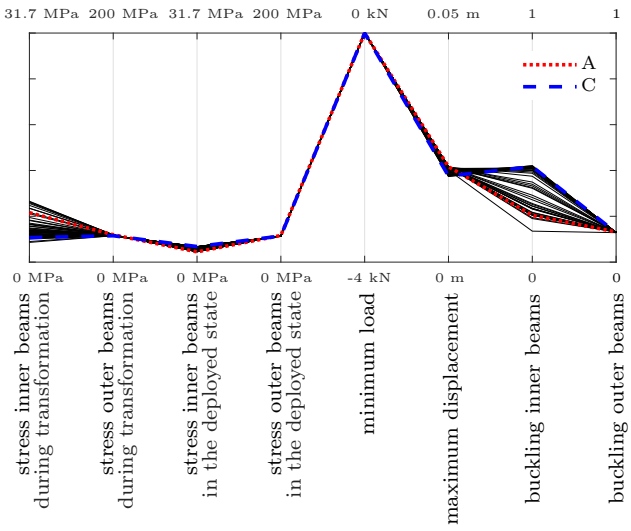

(b) rail BCs

Figure 21: Comparison of the values of the constraints.

sidering a structure with 2 different BCs. For the sake of illustration and ease of comparison, the same structure with beams of 25x25x2 mm has been subjected to the two sets of boundary conditions to investigate the structural behaviour in the deployed state, as well as during transformation. The von Mises stress distributions are given for HDPE and aluminium elements separately (due to a difference in their order of magnitude) in the deployed state (Fig. 22), as well as during transformation (Fig. 23).

The von Mises stress in the HDPE beams in the structure with planar support are generally more evenly distributed, while the stresses in the structure with rail supports are locally higher (Fig. 22). The largest stresses occur in the modules along the two rails of the side rail supported structure, as expected, since they are furthest from the free hanging corner.

The von Mises stress in the aluminium beams for planar supports are negligible in comparison to the stresses in the aluminium beams for rail supports. The highest stress is observed in elements along the side rail supports, as expected. In the deployed state for planar BC, the HDPE beams govern the deflection under self weight, while for side rail support the aluminium beams are critical.

This explains the optimisation results i.e. the solutions for the structure with planar support have large cross sections for the HDPE beams and smaller cross sections for the aluminium beams, while the solutions for the rail support have large cross sections for the aluminium beams and very small cross sections for the HDPE beams.

In Fig. 23a and Fig. 23b, the von Mises stress in the inner HDPE beams is shown in an intermediate configuration during transformation. The stresses in the beams are very similar for the two BCs, which is expected to lead to a similar bistable behaviour of the two structures during transformation.

Fig. 23c and Fig. 23d show the von Mises stress in the outer aluminium beams at the same state of transformation. The stresses in the outer beams for the planar support BC are very small compared to the rail support. The highest stresses in the roof with rail support occur again along the side rail supports.

Fig. 24 compares the load-displacement curves for the same structure with different BCs, showing that the two BCs lead to *a very similar response*, as expected. It is important to emphasize that the considered structure is not a solution of the optimisation problem (e.g. no negative load is present), their purpose is solely to illustrate the difference in the structural behaviour, and link it to the optimisation results.

The optimisation of the roof with rail support gives significantly different results than when considering planar support BCs. This is an expected result because the stress distribution in the two structures is very different. *The difference in the structural behaviour in the deployed state appears to govern the optimisation which explains the very different optimal solutions for different BCs.* This implies that in the design the whole structure has to be optimised in a general setting and that *the results of the optimisation of a single module cannot be used systematically to design a multi-module structure.*

6. Conclusions

Bistable scissor structures should be lightweight, easy to deploy and provide enough stiffness in the deployed configuration to sustain their self-weight. To find acceptable compromises between these conflicting requirements, an optimisation methodology was proposed in which the peak force during deployment as well as the deflection in the deployed state were minimized, taking into account stress based, deflection and buckling constraints. The proposed optimisation approach results in a Pareto front, i.e. several non-dominated solutions, illustrated in this contribution on the example of a single bistable module and a flat roof composed of 5 by 5 modules. This optimisation methodology was shown to be a feasible approach for bistable deployable structures and can be the basis of a rigorous design procedure, which will be developed in the future.

It was shown that the Pareto sets resulting from the optimisation of a single module and the optimisation of a 5 by 5 multi-module structure with similar boundary con-

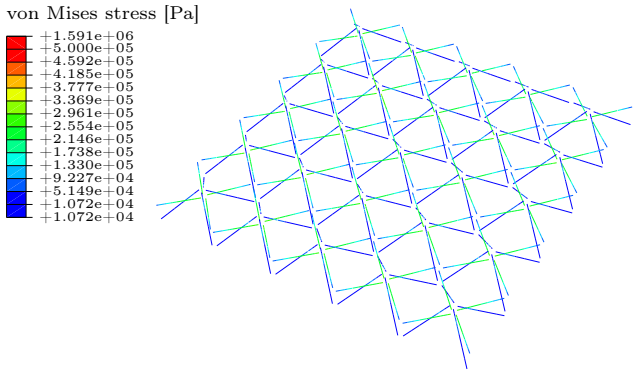

(a) stresses in HDPE, planar support

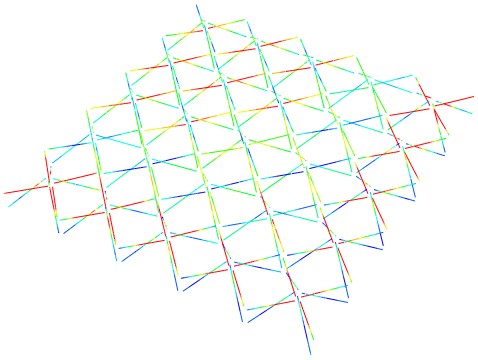

(b) stresses in HDPE, rail support

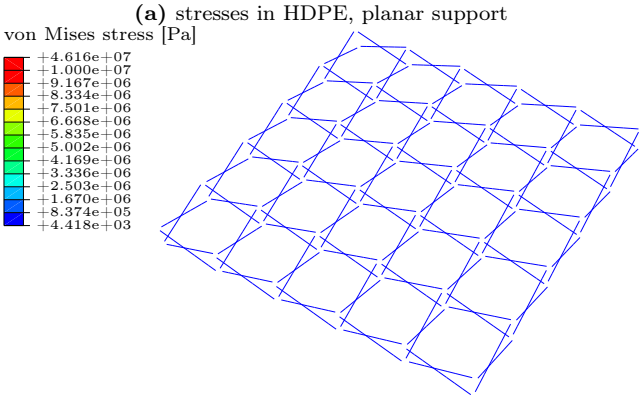

(c) stresses in aluminium, planar support

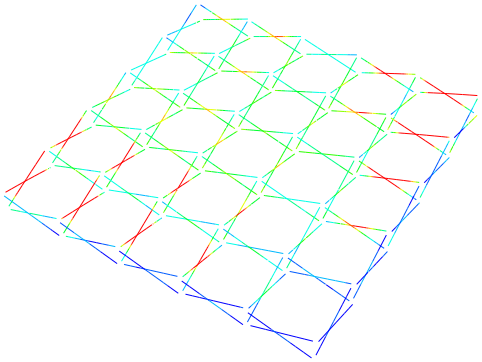

(d) stresses in aluminium, rail support

Figure 22: Comparison of the von Mises stresses in the deployed state.

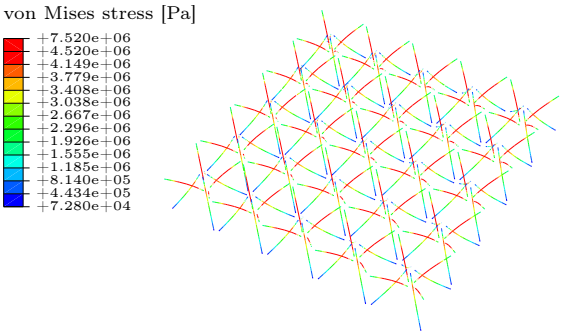

(a) stresses in HDPE, planar support

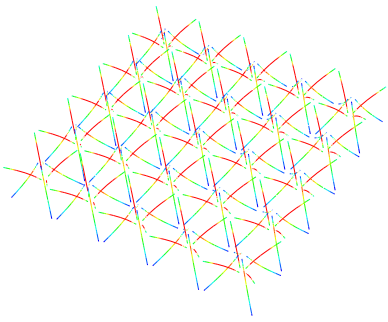

(b) stresses in HDPE, rail support

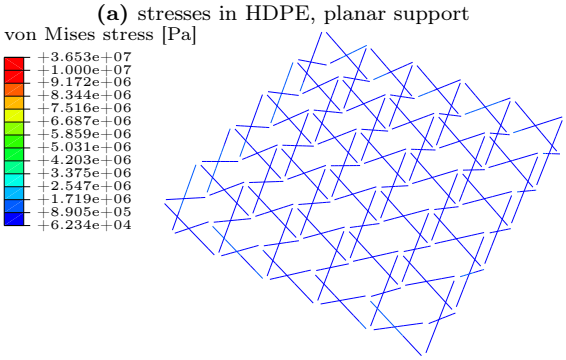

(c) stresses in aluminium, planar support

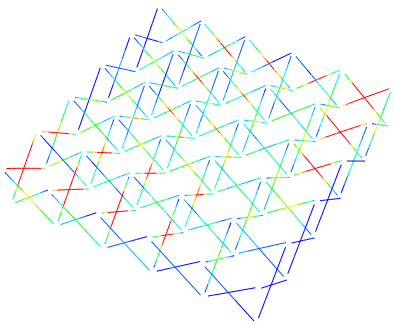

(d) stresses in aluminium, rail support

Figure 23: Comparison of the von Mises stresses during transformation.

ditions (planar support) were very close. It can be concluded that the optimisation of a multi-module structure *can* be deduced from the optimisation of a single module, *provided that the boundary conditions and the applied*

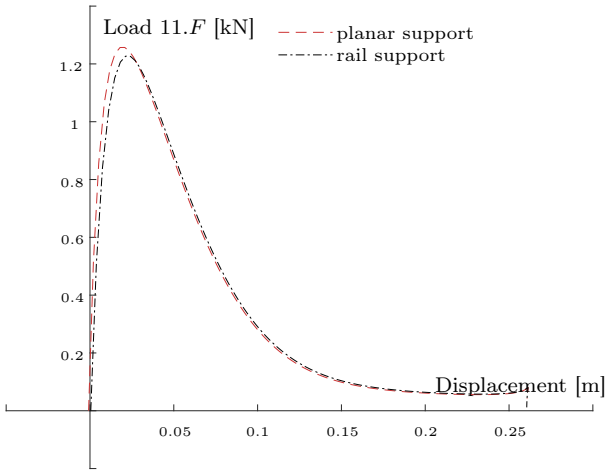

Figure 24: Comparison of the load-displacement curves for different BCs.

loads are comparable. It was shown that for other boundary conditions, i.e. the rail support BC, the results were significantly different. This implies that the whole structure has to be considered in a general setting and that the results of the optimisation of a single module cannot be used in all scenarios.

The main drawback of the current optimisation methodology is the long time and computational effort it takes to obtain a converged Pareto front, which has two causes. First, there is the problem with smoothness of the Pareto fronts, which can be solved by decreasing the maximum arc increment. In the future, an automatic decrease of maximum arc length increment in the Riks path following strategy can be aimed for, to make the process fully automated. Second, for every individual, one linear as well as one non-linear FE simulation is needed. For the case of the pure HDPE single module with 340 generations of 100 individuals, 34,000 linear and 34,000 non-linear FE simulations are required with a computational time of 42 hours on a personal laptop (2.9 GHz intel i7 processor and 32 GB RAM). To reduce the computational time, in the future the non-linear FE simulations can be carried out using displacement control in which it is possible to have smaller load increments in the first part of the load-displacement curve to approximate the peak load more accurately while increasing the load increments in the last part of the curve.

A further extension intended for future work is that the deployed structure will have a more realistic size and boundary conditions and will be subjected to additional loads, in order to demonstrate its applicability for a wider range of applications.

Acknowledgement

This work was supported by a Research Fellow (ASP - Aspirant) fellowship of the Fund for Scientific Research - FNRS (F.R.S.-FNRS) (Grant No. FC 23469).

References

[1] T. R. Zeigler, Collapsible self-supporting structure, United States Patent, US 3,968,808 (1976).
URL https://patents.google.com/patent/US3968808A

[2] T. R. Zeigler, Collapsible self-supporting structures, United States Patent, US 4,026,313 (1977).
URL https://patents.google.com/patent/US4026313A

[3] R. Clarke, The kinematics of a novel deployable space structure system, in: Proceedings of the 3rd International Conference on Space Structures, Elsevier Applied Science Publishers, Guildford, UK, 1984, pp. 820–822. doi:10.1016/0141-0296(87)90007-1.

[4] A. Krishnapillai, Deployable structures, United States Patent, US 5,167,100 (1992).
URL https://patents.google.com/patent/US5167100A

[5] Y. Rosenfeld, R. D. Logcher, New Concepts for Deployable- Collapsable Structures, International Journal of Space Structures 3 (1) (1988) 20–32. doi:10.1177/026635118800300103.

[6] Y. Rosenfeld, Y. Ben-Ami, R. D. Logcher, A Prototype "Clicking" Scissor-Link Deployable Structure, International Journal of Space Structures 8 (1-2) (1993) 85–95. doi:10.1177/0266351193008001-209.

[7] C. J. Gantes, J. J. Connor, R. D. Logcher, Y. Rosenfeld, Structural Analysis and Design of Deployable Structures, Computers and Structures 32 (3-4) (1989) 661–669. doi:10.1016/0045-7949(89)90354-4.

[8] C. J. Gantes, J. J. Connor, R. D. Logcher, Combining numerical analysis and engineering judgment to design deployable structures, Computers and Structures 40 (2) (1991) 431–440. doi:10.1016/0045-7949(91)90368-V.

[9] C. J. Gantes, J. J. Connor, R. D. Logcher, A Systematic Design Methodology for Deployable Structures, International Journal of Space Structures 9 (2) (1994) 67–86. doi:10.1177/026635119400900202.

[10] C. J. Gantes, A. Giakoumakis, P. Vousvounis, Symbolic manipulation as a tool for design of deployable domes, Computers & Structures 64 (1-4) (1997) 865–878. doi:10.1016/S0045-7949(96)00433-6.

[11] C. J. Gantes, Deployable Structures: Analysis and Design, WIT Press, Southampton, UK, 2001. isbn: 1-85312-660-8.

[12] C. J. Gantes, Geometric design of arbitrarily curved bi-stable deployable arches with discrete joint size, International Journal of Solids and Structures 41 (20) (2004) 5517–5540. doi:10.1016/j.ijsolstr.2004.04.030.

[13] K. Kawaguchi, T. Sato, X. Yang, N. Seo, Development of a deployable geodesic full sphere, Journal of the International Association for Shell and Spatial Structures 60 (1) (2019) 35–46. doi:10.20898/j.iass.2019.199.033.

[14] D. S.-H. Lee, O. P. Larsen, O. Popovic, S.-d. Kim, Design of Deployable Structure for Dome Type Emergency Shelter, in: Proceedings of the IASS-SLTE 2014 Symposium - Shells, Membranes and Spatial Structures: Footprints, Brasilia, 2014.
URL https://www.ingentaconnect.com/content/iass/piass/2014/00002014/00000004/art00001

[15] D. S.-H. Lee, W. Jia, J. Cai, A. Malcangi, Investigation into possible geometrical configurations for scissor-type deployable structures using expandable bars, in: Proceedings of the IASS 2015 Symposium - Future Visions, Amsterdam, 2015.
URL https://www.ingentaconnect.com/content/iass/piass/2015/00002015/00000015/art00003

[16] D. Lee, O. Larsen, S. Kim, Computation tools for the design of a deployable dome structure, CRC Press/Balkema, Leiden, The Netherlands, 2016, pp. 267–274. isbn: 978–1–138–02651–3.

[17] K. Roovers, N. De Temmerman, Geometric design of deployable scissor grids consisting of generalized polar units, Journal of the International Association for Shell and Spatial Structures 58 (193) (2017) 227–238. doi:10.20898/j.iass.2017.193.865.

[18] L. I. W. Arnouts, T. J. Massart, N. De Temmerman, P. Z. Berke, Computational modelling of the transformation of bistable scissor structures with geometrical imperfections, Engineering

Structures 177 (2018) 409–420. doi:10.1016/j.engstruct.2018.08.108.

[19] L. I. W. Arnouts, T. J. Massart, N. De Temmerman, P. Z. Berke, Computational design of bistable deployable scissor structures: trends and challenges, Journal of the International Association for Shell and Spatial Structures 60 (199) (2019) 19–34. doi:10.20898/j.iass.2019.199.031.

[20] C. J. Gantes, Overview of scissor-type, bi-stable deployable structures, in: Proceedings of the IASS Symposium 2018 - Creativity in Structural Design, Boston, 2018.
URL https://www.ingentaconnect.com/content/iass/piass/2018/00002018/00000014/art00015

[21] C. J. Gantes, A Design Methodology for Deployable Structures, Ph.D. thesis, Department of Civil Engineering, Massachusetts Institute of Technology (1991).
URL http://hdl.handle.net/1721.1/13901

[22] Z. You, Sensitivity Analysis Based on the Force Method for Deployable Cable-Stiffened Structures, Engineering Optimization 29 (1-4) (1997) 429–441. doi:10.1080/03052159708941006.

[23] A. Kaveh, A. Jafarvand, M. A. Barkhordari, Optimal Design of Pantograph Foldable Structures, International Journal of Space Structures 14 (4) (1999) 295–302. doi:10.1260/0266351991494911.

[24] A. Kaveh, S. Shojaee, Discrete-Sizing Optimal Design of Scissor-Link Foldable Structures Using Genetic Algorithm, Asian Journal of Civil Engineering (Building and Housing) 4 (2-4) (2003) 115–133. doi:10.4203/ccp.80.94.

[25] A. Kaveh, S. Shojaee, Optimal Design of Scissor-Link Foldable Structures Using Ant Colony Optimization Algorithm, Computer-Aided Civil and Infrastructure Engineering 22 (1) (2007) 56–64. doi:10.1111/j.1467-8667.2006.00470.x.

[26] A. Kaveh, S. Talatahari, A hybrid particle swarm and ant colony optimization for design of truss structures, Asian Journal of Civil Engineering 9 (4) (2008) 329—-348.
URL https://ajce.bhrc.ac.ir/Portals/25/PropertyAgent/2905/Files/6183/329.pdf

[27] A. Kaveh, S. Talatahari, A particle swarm ant colony optimization for truss structures with discrete variables, Journal of Constructional Steel Research 65 (8-9) (2009) 1558–1568. doi:10.1016/j.jcsr.2009.04.021.

[28] A. P. Thrall, Design and optimization of linkage-based movable bridge forms, Phd thesis, Department of Civil and Environmental Engineering, Princeton University (2011).
URL https://pqdtopen.proquest.com/doc/879743357.html?FMT=ABS

[29] A. P. Thrall, S. Adriaenssens, I. Paya-Zaforteza, T. P. Zoli, Linkage-based movable bridges: Design methodology and three novel forms, Engineering Structures 37 (2012) 214–223. doi:10.1016/j.engstruct.2011.12.031.

[30] A. P. Thrall, M. Zhu, J. K. Guest, I. Paya-Zaforteza, S. Adriaenssens, Structural Optimization of Deploying Structures Composed of Linkages, Journal of Computing in Civil Engineering 28 (3) (2014) 04014010–1–11. doi:10.1061/(asce)cp.1943-5487.0000272.

[31] L. Alegria Mira, A. P. Thrall, N. De Temmerman, The universal scissor component: Optimization of a reconfigurable component for deployable scissor structures, Engineering Optimization 48 (2) (2015) 317–333. doi:10.1080/0305215x.2015.1011151.

[32] EN 1999-1-1, Eurocode 9: Design of aluminium structures - Part 1-1: General Structural rules, 2007. doi:10.3403/30047501.

[33] L. Alegria Mira, Parametric Structural Assessment of Deployable Scissor Systems. Optimising the Universal Scissor Component, Ph.D. thesis, Vrije Universiteit Brussel. isbn: 978-94-6197-241-5 (2014).

[34] A. Koumar, T. Tysmans, N. De Temmerman, R. Filomeno Coelho, L. Alegria Mira, Multi-criteria optimisation of a barrel vault structure for emergency relief, in: Proceedings of the IASS-SLTE 2014 Symposium - Shells, Membranes and Spatial Structures: Footprints, 2014.
URL https://www.ingentaconnect.com/content/iass/piass/2014/00002014/00000014/art00006

[35] A. Koumar, T. Tysmans, R. Filomeno Coelho, N. De Temmerman, An Automated Structural Optimisation Methodology for Scissor Structures Using a Genetic Algorithm, Applied Computational Intelligence and Soft Computing 2017 (2017) 1–13. doi:10.1155/2017/6843574.

[36] M. Salar, M. R. Ghasemi, B. Dizangian, Practical optimization of deployable and scissor-like structures using a fast GA method, Frontiers of Structural and Civil Engineering 13 (3) (2019) 557–568. doi:10.1007/s11709-018-0497-z.

[37] C. J. Gantes, P. G. Georgiou, V. K. Koumousis, Optimum design of deployable structures using genetic algorithms, Transactions on the Built Environment 35 (1998) 255–264. doi:10.2495/SM980231.

[38] H. Gao, P. Breitkopf, R. F. Coelho, M. Xiao, Categorical structural optimization using discrete manifold learning approach and custom-built evolutionary operators, Structural and Multidisciplinary Optimization 58 (1) (2018) 215–228. doi:10.1007/s00158-017-1890-2.

[39] Y. Tian, R. Cheng, X. Zhang, Y. Jin, PlatEMO: A MATLAB platform for evolutionary multi-objective optimization, IEEE Computational Intelligence Magazine 12 (4) (2017) 73–87. doi:10.1109/MCI.2017.2742868.

[40] A. Koumar, Deployable scissor structures for disaster relief - multi-criteria optimisation and design for adaptability, Ph.D. thesis, Vrije Universiteit Brussel. isbn: 978-9-49231-220-4 (2016).

[41] R. M. . Associates, Rhinoceros 5 [computer software] (2017).
URL http://www.rhino3d.com

[42] Dassault Systèmes, Abaqus 6.12 Analysis User's Manual Volume III: Materials (2012).
URL http://dsk-016-1.fsid.cvut.cz:2080/v6.12/books/usb/default.htm